

Distinct Dimerization for Various Alloforms of the Amyloid-Beta Protein: $\text{A}\beta_{1-40}$, $\text{A}\beta_{1-42}$, and $\text{A}\beta_{1-40}(\text{D23N})$

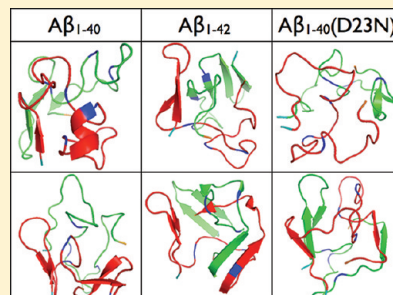
Sébastien Côté,[†] Rozita Laghaei,[†] Philippe Derreumaux,[‡] and Normand Mousseau*,[†]

[†]Département de Physique and Groupe de recherche sur les protéines membranaires (GEPROM), Université de Montréal, C.P. 6128, succursale Centre-ville, Montréal (Québec), Canada

[‡]Laboratoire de Biochimie Théorique, UPR 9080 CNRS, Institut de Biologie Physico-Chimique, Université Paris Diderot, Paris 7 and Institut Universitaire de France, 13 rue Pierre et Marie Curie, 75005 Paris, France

Supporting Information

ABSTRACT: The Amyloid-beta protein is related to Alzheimer's disease, and various experiments have shown that oligomers as small as the dimer are cytotoxic. Two alloforms are mainly produced: $\text{A}\beta_{1-40}$ and $\text{A}\beta_{1-42}$. They have very different oligomer distributions, and it was recently suggested, from experimental studies, that this variation may originate from structural differences in their dimer structures. Little structural information is available on the $\text{A}\beta$ dimer, however, and to complement experimental observations, we simulated the folding of the wild-type $\text{A}\beta_{1-40}$ and $\text{A}\beta_{1-42}$ dimers as well as the mutated $\text{A}\beta_{1-40}(\text{D23N})$ dimer using an accurate coarse-grained force field coupled to Hamiltonian-temperature replica exchange molecular dynamics. The D23N variant impedes the salt-bridge formation between D23 and K28 seen in the wild-type $\text{A}\beta$, leading to very different fibrillation properties and final amyloid fibrils. Our results show that the $\text{A}\beta_{1-42}$ dimer has a higher propensity than the $\text{A}\beta_{1-40}$ dimer to form β -strands at the central hydrophobic core (residues 17–21) and at the C-terminal (residues 30–42), which are two segments crucial to the oligomerization of $\text{A}\beta$. The free energy landscape of the $\text{A}\beta_{1-42}$ dimer is also broader and more complex than that of the $\text{A}\beta_{1-40}$ dimer. Interestingly, D23N also impacts the free energy landscape by increasing the population of configurations with higher β -strand propensities when compared against $\text{A}\beta_{40}$. In addition, while $\text{A}\beta_{1-40}(\text{D23N})$ displays a higher β -strand propensity at the C-terminal, its solvent accessibility does not change with respect to the wild-type sequence. Overall, our results show the strong impact of the two amino acids Ile41-Ala42 and the salt-bridge D23–K28 on the folding of the $\text{A}\beta$ dimer.



INTRODUCTION

The hallmark feature of many neurodegenerative diseases such as Parkinson, Huntington, Creutzfeld-Jakob, and Alzheimer is the appearance of β -sheet-rich insoluble filamentous deposits in brain tissues.^{1,2} Alzheimer's disease, for instance, is characterized by the formation of extra- and intracellular deposits respectively composed of the amyloid β and τ proteins. The amyloid β ($\text{A}\beta$) protein, whose aggregation and oligomer deposition are correlated with the degradation of brain tissues,³ exists in many different alloforms that are produced through the cleavage of the amyloid precursor protein (APP). $\text{A}\beta_{1-40}$ and $\text{A}\beta_{1-42}$ are the most abundant in neuritic amyloid plaques,⁴ and the presence of two hydrophobic residues, Ile41 and Ala42, at the C-terminal leads to very distinct oligomer distributions^{5–7} during fibrillation^{8–10} *in vitro*.

While the exact neurotoxic mechanisms for oligomers are still a matter of debate,¹¹ considerable experimental evidence collected over the past decade shows that metastable $\text{A}\beta$ soluble oligomers correlate more with increased neurotoxicity.¹² While the exact size of these oligomers is not completely clear, even the dimer was recently observed to be synaptotoxic.¹³ Both the growth kinetics and toxicity are strongly affected by the exact amino sequence of $\text{A}\beta$ peptides. Higher $\text{A}\beta_{1-42}/\text{A}\beta_{1-40}$ ratio increases toxicity.¹⁴ $\text{A}\beta_{1-40}$ and $\text{A}\beta_{1-42}$ also show distinct

distributions of low order oligomers, which could be due to differences in their dimer equilibrium structures.¹⁵ Mutations can also affect oligomeric growth and the final product. The Iowa familial mutation, $\text{A}\beta_{1-40}(\text{D23N})$, for example, fibrillates into antiparallel β -sheet fibril morphologies without any lag phase,^{16,17} contrary to what is observed with both $\text{A}\beta_{1-40}$ and $\text{A}\beta_{1-42}$, which show a lag phase and parallel organization.^{9,10}

Characterizing the $\text{A}\beta$ dimerization at the molecular level is crucial for understanding the origin of the various aggregation properties for these different alloforms.^{5–10} To date, very little experimental information is available for the dimer because it is aggregation-prone and exists in equilibrium with fibrils, monomers, and higher-order oligomers.^{6,8} Recently, a combined study using photoinduced cross-linking and circular dichroism (CD) on $\text{A}\beta_{1-40}$ showed that the dimerization increases the β -strand propensity and toxicity as compared with the monomer.¹⁸

In the absence of high-resolution structure data such as solution NMR, however, only computer simulations can provide access to detailed structural and kinetic information about the formation of dimers. Until now, the folding of full-length $\text{A}\beta$

Received: December 31, 2011

Revised: March 9, 2012

Published: March 12, 2012

dimers has been little studied. Monte Carlo simulations were recently used with an all-atom force field and an implicit solvent to determine the structural differences between the $\text{A}\beta_{1-42}$ monomer and dimer, and the impact of the mutants F20E, E22G, and E22G/I31E.^{19,20} The conformational differences that are seen involve turns centered in the 20–30 region, hinting at reorganization of this part of the region as a potentially critical step in $\text{A}\beta$ aggregation. Discrete molecular dynamics (DMD) simulations with a four-bead coarse-grained potential showed an increase of β -strand propensity during the dimerization of $\text{A}\beta_{1-42}$ and $\text{A}\beta_{1-40}$.^{21,22} Shorter $\text{A}\beta$ peptides were also studied. A replica-exchange MD (REMD) simulation on the truncated $\text{A}\beta_{10-40}$, with CHARMM force field and implicit solvent, suggests that the dimer is more extended than the monomer due to interstrand contacts.²³ Another REMD simulation using a coarse-grained potential shows that the $\text{A}\beta_{16-35}$ monomer and dimer are mostly random coil with low secondary structure signals.²⁴ The same potential was also used to simulate the C-terminal fragment $\text{A}\beta_{29-42}$.²⁵ Various simulations were also done on the folding of the full-length $\text{A}\beta$ monomer.^{19,26–29}

More simulations on the full-length $\text{A}\beta$ dimer including the N-terminal segment (residues 1–16) are needed for three reasons. (1) Mutations¹⁸ or deletions⁵ at the N-terminal impact oligomerization, and recent experimental and numerical results on an annular morphology of $\text{A}\beta_{1-42}$ suggest that this segment might not be unstructured³⁰ as opposed to previous observations.⁹ (2) Unknown structures of the $\text{A}\beta$ dimer are cytotoxic¹³ and are important building blocks for higher order oligomers;¹⁵ understanding the structural features of the dimer would help in designing more efficient inhibitors.³¹ (3) While few folding simulations were done on $\text{A}\beta_{1-40}$ ³² and $\text{A}\beta_{1-42}$,²⁰ the only comparison between these sequences was performed using a simple four-bead per residue model with discrete molecular dynamics.²² Moreover, no simulation, to our knowledge, was performed on $\text{A}\beta_{1-40}$ (D23N)'s oligomers.

This is why, following our work on the three full-length monomers,²⁹ we chose to investigate the dimerization of $\text{A}\beta_{1-40}$, $\text{A}\beta_{1-42}$, and $\text{A}\beta_{1-40}(\text{D}23\text{N})$ using the coarse-grained OPEP force field, which has been tested on a number of peptides,³³ coupled to the Hamiltonian-temperature replica exchange molecular dynamics, for increased sampling efficiency.³⁴

This manuscript is constructed as follow. After a discussion of the methodology, we analyze the dimer morphologies of $\text{A}\beta_{1-40}$, $\text{A}\beta_{1-42}$, and $\text{A}\beta_{1-40}(\text{D}23\text{N})$. The impact of the addition of the two residues, I41 and A42, and the D23N substitution are discussed with respect to the wild-type $\text{A}\beta_{1-40}$. Finally, we compare our results to previous simulations and experiments, and identify important structural motifs for $\text{A}\beta$ dimerization and further aggregation.

METHODS

In this study, we simulated three different alloforms of the amyloid beta protein: $\text{A}\beta_{1-40}$, $\text{A}\beta_{1-42}$, and $\text{A}\beta_{1-40}(\text{D}23\text{N})$ using the OPEP/HT-REMD simulation protocol.³⁴ The amino acid sequence of $\text{A}\beta_{1-40}$ is DAEFRHIDSGYEVHHQKLVF-FAEDVGSNKGAIIGLMVGGVV. For $\text{A}\beta_{1-42}$, two hydrophobic residues, Ile41 and Ala42, are added at the C-terminal. For $\text{A}\beta_{1-40}(\text{D}23\text{N})$, Asp23 is mutated into Asn23, resulting in a side chain without a net negative charge at neutral pH.

To maximize sampling, temperature replica exchange molecular dynamics, T-REMD,³⁵ is combined with Hamiltonian replica exchange molecular dynamics, H-REMD.^{34,36} We use 22 temperatures: 270, 279, 289, 299, 309, 320, 331, 342, 354, 366,

379, 392, 405, 419, 434, 443, 451, 458, 463, 466, 468, and 470 K. At the highest temperature, we fractionally reduce nonbonded attractive forces using four scales: 0.8, 0.6, 0.4, and 0.2. Temperature is controlled using a Berendsen thermostat³⁷ with a coupling constant of 100 fs, the integration time step is 1.5 fs, and exchanges are attempted every 7.5 ps. We save the configurations every 7.5 ps. Bond lengths are constrained with the RATTLE algorithm.³⁸ All simulations are started from a random extended conformation, and each dimer is simulated in a 40 Å-radius sphere with reflecting boundary conditions. Overall, each alloform is simulated for 1250 ns per replica, yielding a total simulation time of 32.5 μs per alloform.

Previously, our simulation protocol, HT-REMD coupled with the OPEP force field, was tested on the $\text{A}\beta_{1-40}$, $\text{A}\beta_{1-42}$, and $\text{A}\beta_{1-40}(\text{D}23\text{N})$ monomers, leading to good agreement with experiments.²⁹ For complementarity, we provide a comparison with the experimental values of the chemical shifts measured on the $\text{A}\beta_{1-40}$ and $\text{A}\beta_{1-42}$ monomers (Supp. Figure 1, Supporting Information).

Force Field. To reach longer time-scales, we chose the implicit coarse-grained OPEP potential (optimized potential for efficient peptide structure prediction), version 3.2, because this force field captures the essential driving forces in protein folding and structure prediction without costing as much computational time as would have an all-atom potential with explicit solvent representation.^{33,39–41} This potential has been shown to recover the native structure of a variety of peptides with widely different secondary and tertiary structures as accurately as all-atom potentials using T-REMD⁴² and greedy^{39,40} simulations. Also, OPEP has been applied to study the aggregation of many short and long amyloid peptides such as amylin,^{34,43} polyglutamine,⁴⁴ GNNQQNY,⁴⁵ KFFE,⁴⁶ and various segments of $\text{A}\beta$.^{24,25,29,47–50} This potential models each amino acid by C, N, N_H , C_ω , O and a single bead (SC) for the side chain. The properties of each side chain are unique, and their parameters are finely tuned against thermodynamics and protein structures determined experimentally as described previously.³³ The OPEP force field includes bonded interactions such as bond lengths, bond angles, improper torsion angles, and dihedral angles and nonbonded interactions such as van der Waals and two-body and four-body hydrogen bond potentials.

HT-REMD. Hamiltonian-temperature replica exchange molecular dynamics, HT-REMD,³⁴ is a hybrid of the popular temperature replica exchange molecular dynamics, T-REMD,³⁵ and Hamiltonian replica exchange molecular dynamics, H-REMD.³⁶ Preliminary tests on the $\text{A}\beta_{1-42}$ dimer with the OPEP force field showed that, even at very high temperature, the two chains would keep intermolecular interactions, preventing a complete sampling of the conformational space. To reduce this bias, we use a H-REMD scheme at the highest temperature in which we fractionally reduce nonbonded attractive forces, favoring a more complete dissociation of the two chains enhancing conformation space sampling when these replicas move back to lower temperatures. The algorithm has been previously detailed.^{29,34}

Analysis. We analyze the secondary and tertiary structures of $\text{A}\beta_{1-40}$, $\text{A}\beta_{1-42}$, and $\text{A}\beta_{1-40}(\text{D}23\text{N})$ at 300 K. Secondary structures are predicted using STRIDE.⁵¹ Tertiary structures are analyzed from the network of side chain contacts. Here, a contact is considered formed when two side-chain beads are separated by a distance that is less than the sum of their van der Waals radii plus 0.5 Å. To further characterize and extract the relevant morphologies, we employ a two-step clustering

procedure. First, the morphologies are regrouped using a rmsd metric with Daura's procedure⁵² that finds the biggest cluster, then removes these configurations, and repeats iteratively until no structure is left. We chose a relatively selective C_{α} -rmsd threshold of 2 Å, to provide first screening. Second, all cluster centers are reclustered according to the homology between their contact network using a threshold of 75% homology. In each clustering step, the permutation of the two chains is checked. Molecular graphics images were generated using the PyMOL software (<http://www.pymol.org/>). To complement our analysis on the tertiary structure, we also calculated the solvent accessible surface area⁵³ per residue on all structures reconstructed to all-atom using Scrwl4.⁵⁴ The thermodynamical properties are calculated by WHAM.⁵⁵ The free energy landscape is calculated by the histogram analysis method using two reaction coordinates: the percentage of β -strand content and the normalized number of hydrophobic contacts, which is defined as the total number of hydrophobic contacts divided by the number of hydrophobic residues in the alloform. The entropy is extracted using the first law of thermodynamics, $F = E - TS$, and the free energy calculated by WHAM.

Convergence. Convergence of the simulation is assessed in the following way. First, we verify that the entropy as a function of temperature $S(T)$ is time-independent when computed over non-overlapping time intervals. This occurs, for the sequences studied here, after 650 ns of simulation at each temperature. Figure 1 shows that $S(T)$ remains unchanged for all alloforms

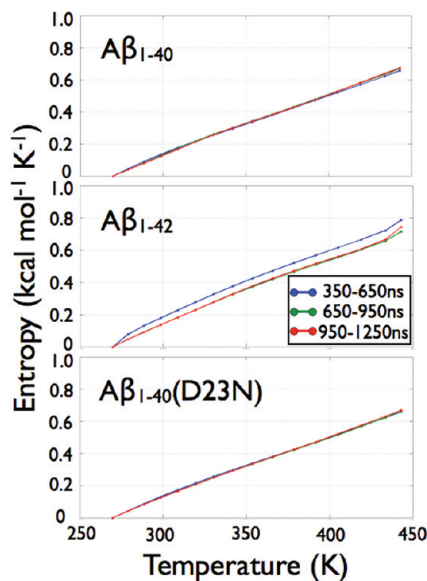


Figure 1. Simulation convergence assessed from the entropy as a function of temperature. From top to bottom, the entropy as a function of temperature for $A\beta_{40}$, $A\beta_{42}$, and $A\beta_{40}(D23N)$ in the time intervals 350–650, 650–950, and 950–1250 ns. The strong similarity between the curves at 650–950 and 950–1250 ns for each alloform suggests that our simulations are converged in the time interval 650–1250 ns.

when computed on the 650–950 and 950–1250 ns time intervals. Second, computing the cluster distributions, the secondary structures per residue, and the contact maps in both time windows, we confirm that secondary and tertiary structures are well converged. Accordingly, the analysis is performed on the 80 000 structures collected within the 650–1250 ns time interval for each alloform.

Naming Convention. We focus our analysis on four segments of the peptide that are known experimentally to have a role during the oligomerization:^{5,6} the N-terminal (residues 1–16), the central hydrophobic core (CHC) (residues 17–21), the fibril-loop region (residues 22–28), and the C-terminal (residues 29–40/42). The N-terminal and the fibril-loop region are mostly hydrophilic, while the CHC and the C-terminal are mostly hydrophobic. In the final amyloid fibril products of the three alloforms, the fibril-loop region forms a loop, and both the CHC and C-terminal form β -sheets, whereas the N-terminal is mostly disordered.^{9,10,17} To simplify the notation in the Results and Discussion sections, we abbreviate $A\beta_{1-40}$, $A\beta_{1-42}$, and $A\beta_{1-40}(D23N)$ by $A\beta_{40}$, $A\beta_{42}$, and $A\beta_{40}(D23N)$, respectively.

RESULTS

Dimerization of $A\beta_{40}$. *Secondary Structure.* The averaged secondary structure propensities over all residues are shown in Table 1. We observe that the $A\beta_{40}$ dimer mostly

Table 1. Secondary Structure Averaged over All Residues and Structures^a

secondary structure (%)	$A\beta_{40}$		$A\beta_{42}$		$A\beta_{40}(D23N)$	
	monomer	dimer	monomer	dimer	monomer	dimer
α -helix	6.0	1.3	4.7	4.4	0.9	0.2
β -strand	11.8	12.6	10.8	30.8	15.9	10.7
turn	44.8	50.7	44.8	32.4	55.1	52.3
random coil	37.4	35.4	39.8	32.4	28.0	36.6

^aThe values shown for the dimer are averaged over the converged interval (see the Methods section). The monomer results were taken at 300 K from our previous study on the full-length $A\beta_{40}$, $A\beta_{42}$, and $A\beta_{40}(D23N)$ monomers.²⁹ The statistical errors are small, <0.1%, according to the interval of confidence on the mean value given by a Bootstrap analysis.

populates turn/random coil with 12.6% of β -strand. The secondary structure per residue reveals that it is not distributed uniformly. The β -strands are mostly localized in three regions: the N-terminal with more than 10% and up to 80% (residues 2–6 and 9–16) and the fibril-loop region and the C-terminal (residues 23–28 and 36–38) with 5–10%, while the CHC has a weak β -strand propensity that is smaller than 2% (Figure 2). α -Helices are only populated in the fibril-loop region (5–10%). Finally, residues 7–9, 13–15, 21–28, and 33–39 show a significant propensity for turns, larger than 50%.

Contacts. The networks of total, intrachain, and interchain contacts of the $A\beta_{40}$ dimer are shown in Figure 3 (first column). We see that the region of highest contact density involves hydrophobic interactions between the CHC (residues 17–20) and the C-terminal (residues 31–36). Other regions with a notable high contact density are CHC/CHC (residues 17–20/17–20) and C-terminal/C-terminal (residues 36–40/31–36). From the intra- and interchain contact maps (panels below), we note that the interactions at the CHC/C-terminal occur both intra and between chains, while CHC/CHC contacts are almost exclusively interchain. The D23–K28 salt-bridge is present intramolecularly in 55.2% of the configurations, while it is weakly populated intermolecularly with 4.7% propensity (Table 2). Interestingly, there are few contacts, intra- or intermolecular, between the N-terminal and the C-terminal. For example, residues 1–16 interact with residues

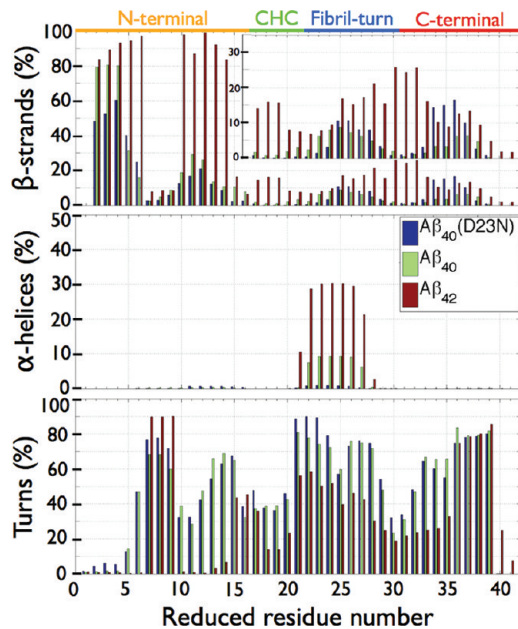


Figure 2. Per residue secondary structure. From top to bottom, β -strands, α -helices, and turn propensities for $A\beta_{40}$ (green), $A\beta_{42}$ (red), and $A\beta_{40}(D23N)$ (blue).

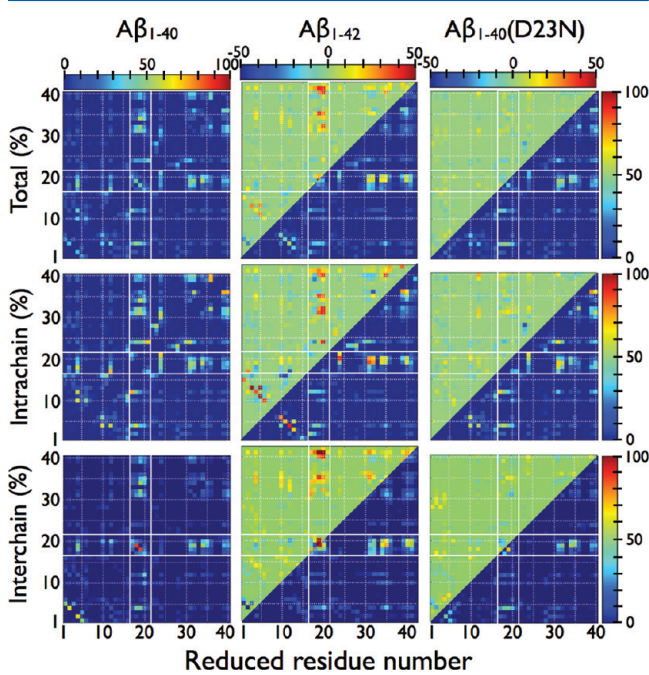


Figure 3. Network of side-chain contacts. The percentages of total (first row), intrachain (second row), and interchain (third row) contacts are depicted. The total contact propensity is calculated from % intra plus % inter. The first column shows the values for the $A\beta_{40}$ dimer, and the bottom-right corner maps of the second and third columns show the values for the $A\beta_{42}$ and $A\beta_{40}(D23N)$ dimers, respectively. The dimers of $A\beta_{42}$ (second column) and $A\beta_{40}(D23N)$ (third column) are compared to the dimer of $A\beta_{40}$ in the top-left corner maps. The percentage difference is calculated from the % in the $A\beta_{42}$ or $A\beta_{40}(D23N)$ dimers minus the % in the $A\beta_{40}$ dimer. The white lines, which are found between residues 16 and 17 and between residues 21 and 22, delimit the CHC region.

1–21, while they have few contacts with residues 22–40 (fibril-loop region and C-terminal).

Table 2. Propensities of K28–D23 and K28–E22 Contacts^a

contact (%)	$A\beta_{40}$		$A\beta_{42}$		$A\beta_{40}(D23N)$	
	intra	inter	intra	inter	intra	inter
K28–E22	35	4	27	0	29	3
K28–D(N)23	55	5	54	0	14	1
K28–other D or E	8	4	4	6	7	11
K28–E22	+12		-17		-6	
K28–D(N)23	-18		-18		-1	
K28–other D or E	-12		-9		-4	

^aRows 1–3 show the propensities of intra- and intermolecular contacts between K28 and D(N)23 or E22 in the $A\beta_{40}$, $A\beta_{42}$, and $A\beta_{40}(D23N)$ dimers. Rows 4–6 show the difference in propensities between the dimer and the monomer (% dimer minus % monomer). The values shown for the dimer are extracted from Figure 2. The monomer results were taken at 300 K from our previous study on the $A\beta_{40}$, $A\beta_{42}$, and $A\beta_{40}(D23N)$ monomers.²⁹ The third and sixth rows show the mean contact propensities between K28 and D1, E3, D7, or E11, which are the other negatively charged residues in $A\beta$. The statistical errors are small, <1%, according to the interval of confidence on the mean value given by a Bootstrap analysis.

Clusters. To complement the analysis on the tertiary structure, we look at the six principal morphologies of the $A\beta_{40}$ dimer totaling 49% of its recorded structures (first column of Figure 4). The secondary structures of the six clusters are shown in Table 3. We see that these morphologies display various β -sheets at the N-terminal and are rather unstructured elsewhere, although some structural motifs are seen. For instance, the third and fifth clusters have an α -helix at residues 22–26 of the fibril-loop region and the third cluster shows an intramolecular β -sheet in chain 2 between residues 37–38 of the C-terminal and residues 11–13 of the N-terminal. The β -sheets observed in the six dominant clusters are all antiparallel (Table 3).

We also cluster the structures having at least 33% of β -strands at the CHC (two amino acids) or the C-terminal (three amino acids) in either chain, since these marginal morphologies may be more prone to oligomerize.⁵⁶ These structures represent 14% of the total ensemble, and the first six clusters are shown in Figure 5. We see different types of motifs involving the C-terminal: it forms a two-stranded β -sheet with the C-terminal (interchain in cluster 4), the fibril-loop region (intrachain in clusters 2 and 6), or the N-terminal (intrachain in cluster 1 or interchain in cluster 3). On the other hand, the CHC is not involved in any β -sheet with the C-terminal for these clusters; it instead forms a β -sheet with the fibril-loop region (interchain in cluster 5). Only the third cluster shows parallel β -sheets (between the N- and C-terminals), while the other clusters show antiparallel β -sheets (Table 3).

Free Energy Landscape. The free energy landscape, which is plotted as a function of the percentage of β -strand content (x -axis) and the normalized number of hydrophobic contacts (y -axis), is shown in Figure 6 (first row). We observe that most morphologies are found in a region between 4.5 and 5.25 normalized hydrophobic contacts and between 12 and 22% β -strand propensity. There, we observe the three deepest free energy minima, which are centered around 4.8 normalized hydrophobic contacts and 13, 15, and 20% β -strand and which are separated by weak free energy barriers (1.2 and 0.8 kcal/mol, respectively). Morphologies with a β -strand propensity higher than 25% are sparsely populated.

Dimerization of $A\beta_{42}$. Secondary Structure. The $A\beta_{42}$ dimer has a much higher β -strand propensity (31%) than the $A\beta_{40}$ dimer (13%), as shown in Table 1. This gain leads to an

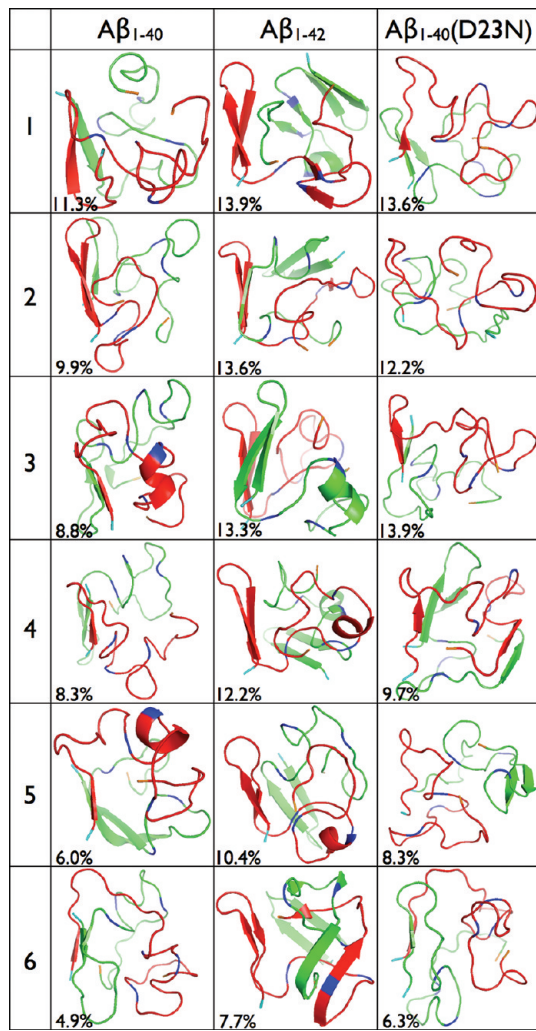


Figure 4. Dominant morphologies. The six main clusters' centers are shown for $\text{A}\beta_{40}$ (first column), $\text{A}\beta_{42}$ (second column), and $\text{A}\beta_{40}(\text{D}23\text{N})$ (third column). The N-terminal and the C-terminal are shown in teal and orange, respectively. The first residue in each of the peptide regions is shown in blue: Leu17 (CHC), Glu22 (fibril-loop region), and Ala30 (C-terminal). The first chain is shown in red, and the second, in green.

equivalent reduction in turn propensity that falls to 32%. This leaves 32% random coil and 4% α -helix, which are similar to $\text{A}\beta_{40}$ propensities. The $\text{A}\beta_{42}$ dimer enhances the formation of β -strands at the expense of turns for almost all residues when compared to the $\text{A}\beta_{40}$ dimer (Figure 2). Residues 2–6 and 10–14 of the N-terminal populate β -strands with 80% probability or more. The β -strand propensity is 7–15% at residues 17–21 (CHC) and 10–25% at residues 25–38 (fibril-loop region and C-terminal), which is higher than $\text{A}\beta_{40}$, as this alloform shows <2% (CHC) and 5–10% (C-terminal). The turn propensity of $\text{A}\beta_{42}$ is lower than $\text{A}\beta_{40}$ for all residues except for residues 7–9. For example, the turn at residues 13–15, which is present in $\text{A}\beta_{40}$, is absent from $\text{A}\beta_{42}$. The resulting turn distribution with a propensity greater than 50% is thus more localized to residues 7–9, 21–24, and 36–39 (Figure 2). On the other hand, as for $\text{A}\beta_{40}$, the $\text{A}\beta_{42}$ dimer exhibits a polymorphic fibril-loop region displaying α -helix, β -strand, turn, and random coil in competition.

Contacts. Contact maps for $\text{A}\beta_{42}$ are provided in Figure 3 (second column). Similarly to $\text{A}\beta_{40}$, the highest contact density

region is localized at the CHC/C-terminal region (residues 17–20/31–41). The other notable regions of high contact density are CHC/CHC (residues 17–20/17–20) and C-terminal/C-terminal (residues 31–36/34–41) (top row). The main difference resides in that this alloform has more contacts overall than the $\text{A}\beta_{40}$ dimer. More precisely, hydrophobic contact propensities between the following regions are strengthened by the addition of Ile41 and Ala42: CHC/CHC (interchain), CHC/C-terminal (intra- and interchain), and C-terminal/C-terminal (intra- and interchain), as shown in the intrachain and interchain contact maps (middle and bottom rows, respectively). As for the charged residue K28, it displays a slightly reduced propensity for the formation of an intramolecular contact with D23 and a much lower propensity to interact with E22 in the $\text{A}\beta_{42}$ dimer than in $\text{A}\beta_{40}$ (Table 2). Intermolecular contact propensities between K28 and D23 or E22 are very low in $\text{A}\beta_{42}$ as for $\text{A}\beta_{40}$.

Clusters. As expected from the secondary structure analysis, the clusters of the $\text{A}\beta_{42}$ dimer are more ordered than for the $\text{A}\beta_{40}$ dimer (see the second column of Figure 4). The positions of the secondary structure elements in each cluster are shown in Table 4. The six clusters represent 71% of the 80 000 structures recorded for $\text{A}\beta_{42}$, indicating that, already at the dimer level, $\text{A}\beta_{42}$ cannot be described as fully random coil/turn configurations. In contrast with $\text{A}\beta_{40}$, the N-terminal of these morphologies has a high propensity to populate a β -hairpin motif, and the CHC can be involved in a β -sheet as seen in the first cluster. In the second cluster, the N-terminal of each chain forms a three-stranded β -sheet with the fibril-loop region of the other chain. In the third cluster, the β -hairpin motifs at the N-terminal of each chain interact, forming a quasi four-stranded β -sheet, and an α -helix is formed in the fibril-loop region. The fourth and fifth clusters have an intramolecular two-stranded β -sheet at their N-terminals with an α -helix in the fibril-loop region. Finally, the sixth cluster displays an almost completely extended C-terminal which forms a β -sheet with the fibril-loop region of the other chain. In terms of orientation, the β -sheets observed in these six clusters are all antiparallel (Table 4).

We also look at the morphologies having at least 33% β -strand at the CHC (two amino acids) or C-terminal (four amino acids) in either chain (second column of Figure 5), a criterion that is met by more than 38% of $\text{A}\beta_{42}$ visited morphologies, compared with 14% for $\text{A}\beta_{40}$. Among the important features of this subgroup of conformations, we note an important role for the C-terminal which forms either inter- or intrachain β -sheets with itself (respectively cluster 2 and clusters 4 and 6), as well as with the CHC (intrachain in cluster 1), the fibril-loop region (interchain in clusters 2 and 5), and the N-terminal (interchain in cluster 3). Interestingly, the β -sheet motif between the CHC and C-terminal is not observed for $\text{A}\beta_{40}$. Moreover, the β -sheets at the C-terminal are longer than what is observed for $\text{A}\beta_{40}$ and we see, for instance, a long antiparallel intermolecular β -sheet between the two C-terminals in the fifth cluster. This latter motif is interesting, as one side of this β -stranded C-terminal is completely exposed to the solvent and it might be possible that such a motif promotes, during further oligomerization, the formation of an intermolecular β -sheet with the C-terminal of a third chain. In these six clusters, all β -sheets have an antiparallel orientation (Table 4). Finally, we note that no α -helix is observed in these clusters for $\text{A}\beta_{42}$ as opposed to $\text{A}\beta_{40}$.

Free Energy Landscape. The free energy profile for the $\text{A}\beta_{42}$ dimer is shown in Figure 6 (second row). It shows that most

Table 3. Secondary Structure of $\text{A}\beta_{40}$ Dominant Morphologies^a

cluster no.	clusters in Figure 4		clusters in Figure 5	
	res. no. (chain no.)	motif	res. no. (chain no.)	motif
1	8–12 (#1)/2–6 (#2)	a-p. β	22–27 (#1) 2–4 (#1)/2–4 (#2) 10–12 (#2)/36–38 (#2)	α a-p. β a-p. β
2	2–7 (#1)/11–16 (#1)/2–4 (#2)	a-p. β	2–4 (#1)/10–12 (#1) 25–28 (#1)/34–37 (#1)	a-p. β a-p. β
3	22–26 (#1) 2–4 (#1)/2–4 (#2) 11–13 (#2)/37–38 (#2)	α a-p. β a-p. β	2–4 (#1)/2–4 (#2) 10–12 (#1)/36–38 (#2) 37–38 (#1)/15–16 (#2)	a-p. β p. β p. β
4	2–4 (#1)/2–5 (#2)/11–13 (#2)	a-p. β	9–12 (#1)/2–5 (#2) 34–36 (#1)/34–36 (#2)	a-p. β a-p. β
5	22–26 (#1) 2–4 (#1)/2–11 (#2)/23–27 (#2)	α a-p. β	2–4 (#1)/2–4 (#2) 23–30 (#1)/20–28 (#2)	a-p. β a-p. β
6	2–4 (#1)/2–4 (#2)/14–15 (#2)	a-p. β	2–4 (#1)/10–12 (#1) 25–28 (#1)/34–37 (#1)	a-p. β a-p. β

^aThe clusters of Figure 4 represent the dominant morphologies, while the clusters of Figure 5 represent the dominant morphologies having at least 33% β -strand content at the CHC or at the C-terminal. The motifs indicated in the table are α -helix (α) and anti-parallel (a-p.) and parallel (p.) β -sheets (β).

morphologies have between 5.25 and 6.5 hydrophobic contacts per hydrophobic residue and 15–60% β -strand propensity. As a result, the phase space visited is shifted toward more hydrophobic contacts and higher β -strand contents than in $\text{A}\beta_{40}$, in agreement with our analysis of their secondary structures, contact propensities, and clusters. In detail, the two deepest free energy minima, which are separated by a ~ 0.9 kcal/mol energy barrier, are found in a region between 5.25 and 6.5 normalized hydrophobic contacts and 22–32% β -strands. Other important free energy minima, which are separated by higher energy barriers (~ 1.5 kcal/mol), are found at higher β -strand contents, namely, at 35–40, % and 55–59%. A shallower minimum is found at even higher β -strand content (62–63%). The addition of Ile41 and Ala42 in $\text{A}\beta_{42}$ energetically favors morphologies with higher hydrophobic contact propensity per hydrophobic residue (>5.5) and β -strand propensity (>30%) than in $\text{A}\beta_{40}$. Overall, the free energy landscape of the $\text{A}\beta_{1–42}$ dimer is broader and more complex than that of the $\text{A}\beta_{1–40}$ dimer.

Are These Morphologies Stable for the $\text{A}\beta_{40}$ Dimer? We previously showed that the $\text{A}\beta_{42}$ and $\text{A}\beta_{40}$ dimers visit very different morphologies. To ensure that this difference is real and not associated with sampling limitations, we truncated the last two C-terminal residues, Ile41 and Ala42, from the 22 + 4 replicas of the $\text{A}\beta_{42}$ dimer HT-REMD in the middle of the converge interval, at $t = 925$ ns, and relaunched the simulation to ascertain their stability. After only 25 ns, we observe that the secondary structure of $\text{A}\beta_{42}\Delta(41–42)$ relaxes toward the equilibrated data for $\text{A}\beta_{40}$ at 300 K, the temperature of analysis. To confirm that this is not only a brief structural reorganization, we continued the simulation. After 325 ns, the β -strand, α -helix, and turn distributions have relaxed to the values obtained for $\text{A}\beta_{40}$ (Supp. Figure 2, Supporting Information). The same observation is made at 270 K, the lowest temperature of analysis. The difference observed between the various alloforms is therefore not due to a sampling artifact.

Dimerization of $\text{A}\beta_{40}(\text{D23N})$. **Secondary Structure.** The secondary structure of the $\text{A}\beta_{40}(\text{D23N})$ dimer is shown in Figure 2. While the averaged propensities over all residues for $\text{A}\beta_{40}(\text{D23N})$ are similar to $\text{A}\beta_{40}$ (Table 1), the per residue propensities differ notably. Namely, the β -strand propensity of $\text{A}\beta_{40}(\text{D23N})$ is lower at the N-terminal but higher at residues

34–37, where we observe a lower turn propensity, leading to a more extended C-terminal when compared to WT. The α -helix propensity is also much lower in the fibril-loop region enhancing turn (residues 20–24) and β -strand (residues 25–28) propensities. Overall, the secondary structure distribution of $\text{A}\beta_{40}(\text{D23N})$ can be described by four regions where β -strands are present with propensities greater than 5% (residues 2–6, 9–14, 25–28, and 34–37) and four regions where turns are found with propensities greater than 50% (residues 7–9, 13–15, 21–29, and 33–39). We note, in particular, that residues 17–21 of the CHC are almost free of any β -strand and α -helix propensities.

Contacts. The region with the highest contact density for $\text{A}\beta_{40}(\text{D23N})$ is the CHC/C-terminal (residues 17–20/31–36), as for $\text{A}\beta_{40}$ (Figure 3, third row). The CHC/CHC (residues 17–20/17–20) and C-terminal/C-terminal (residues 36–40/31–36) regions also display high contact density. The mutation D23N causes an overall small increase in the number of inter- and intramolecular contacts, particularly between the CHC/C-terminal regions and the CHC/N-terminal regions. This increase is, however, far less important than what is observed when $\text{A}\beta_{42}$ is compared to $\text{A}\beta_{40}$. In spite of this general rise in contacts, some specific regions show a decrease when compared to WT. This is the case for the interchain contacts between the CHC/CHC regions (residues 17–18/20), as well as for K28, which less frequently forms a contact with D23 that has been mutated to an asparagine (Table 2). Even if freed from this salt bridge, K28 does not interact significantly more with the other negatively charged residues.

Clusters. The first six clusters of $\text{A}\beta_{40}(\text{D23N})$, which represent 64% of its recorded structures, are relatively devoid of secondary structure (Figure 4 and Table 5). The secondary structure elements of its clusters are shown in Table 5. The first cluster only displays a three-stranded β -sheet between residues 2–3 (chain 1), 2–5 (chain 2), and 10–12 (chain 2) at the N-terminal without any other secondary structure. The second cluster is completely disordered, while the third cluster shows only a short β -sheet between residues 2–4 (chain 1) and 2–4 (chain 2). A different motif from the WT main morphologies is observed, however, in the fourth cluster that shows an intermolecular β -sheet at the C-terminal between residues 33–36

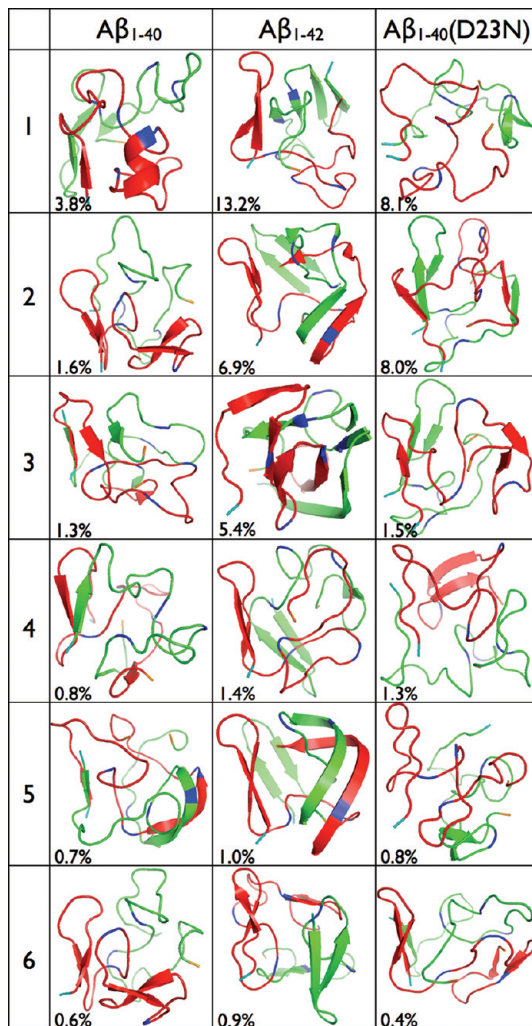


Figure 5. Dominant morphologies having β -strands at the CHC or C-terminal. The centers of the six main clusters having β -strands for more than 33% of the residues at the CHC or at the C-terminal in either chain are shown for $\text{A}\beta_{40}$ (first column), $\text{A}\beta_{42}$ (second column), and $\text{A}\beta_{40}(\text{D}23\text{N})$ (third column). The N-terminal and the C-terminal are shown in teal and orange, respectively. The first residue in each of the peptide regions is shown in blue: Leu17 (CHC), Glu22 (fibril-loop region), and Ala30 (C-terminal). The first chain is shown in red, and the second, in green.

(chain 1) and 34–37 (chain 2) as well as a three-stranded β -sheet at the N-terminal (residues 4–6 of chain 1 and residues 2–6 and 12–14 of chain 2). The C-terminal residues 34–37 of the fifth cluster are also involved in an intramolecular β -sheet with the fibril-loop region (residues 25–28). Finally, the sixth cluster is mostly disordered, as the third cluster, having only a short β -sheet at the N-terminal between residues 2–4 (chain 1) and 4–6 (chain 2). As opposed to the clusters of the other alloforms, some of $\text{A}\beta_{40}(\text{D}23\text{N})$'s clusters display a parallel β -sheet at the N-terminal (clusters 1, 4, and 6), as shown in Table 5. In contrast, the β -sheets involving other parts of the peptide are antiparallel.

The clusters formed from the configurations containing at least 33% β -strand at the CHC (two amino acids) or at the C-terminal (three amino acids) in either chain represent 22% of the $\text{A}\beta_{40}(\text{D}23\text{N})$ structures, which is more than $\text{A}\beta_{40}$ (14%). The first six clusters are shown in Figure 5. We observe that these remain mostly unstructured, similarly to $\text{A}\beta_{40}$, but with a

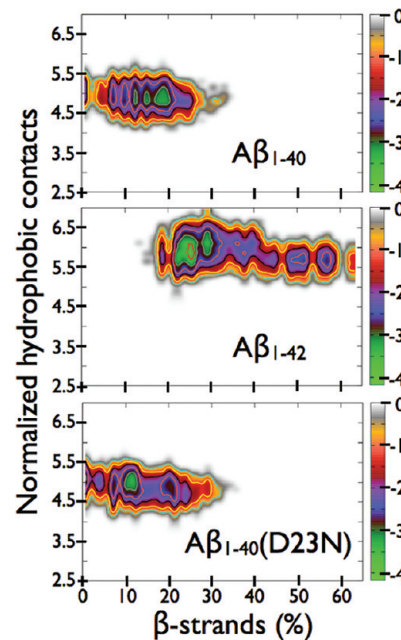


Figure 6. Free energy profile. From top to bottom, the free energy profile in kcal/mol of $\text{A}\beta_{40}$, $\text{A}\beta_{42}$, and $\text{A}\beta_{40}(\text{D}23\text{N})$ projected onto the β -strand content (x -axis) and the normalized number of hydrophobic contacts (y -axis). The normalized number of hydrophobic contacts is calculated from the total number of hydrophobic contacts divided by the number of hydrophobic residues in the alloform.

few original motifs. For example, the first and fifth clusters display a β -hairpin motif between the fibril-loop region (residues 25–28 of chain 2) and C-terminal (residues 34–37 of chain 2), whereas all the other residues are unstructured. A similar motif is observed in the fourth cluster between residues 25–29 and 34–38 in chain 1. In the second cluster, an intermolecular antiparallel β -sheet between the C-terminal is seen (residues 33–36 of chain 1 and residues 34–37 of chain 2). In contrast, similarly to $\text{A}\beta_{40}$ (cluster 6), the C-terminal of the third and sixth clusters interacts with the fibril-loop region as well as having a small β -sheet at the N-terminal. As for the dominant morphologies, these clusters only show antiparallel β -sheets outside the N-terminal, while some parallel organization is observed at the N-terminal (Table 5).

Free Energy Landscape. The free energy profile of $\text{A}\beta_{40}(\text{D}23\text{N})$, which is shown in Figure 6, is more similar to the $\text{A}\beta_{40}$ profile than $\text{A}\beta_{42}$. As $\text{A}\beta_{40}$, most morphologies populated are found between 4.25 and 5.5 hydrophobic contacts per hydrophobic residues and 0–30% β -strand propensity. However, the minima layout exhibits striking differences. There are two free energy basins (around 6–15 and 18–22% β -strand content) that are separated by a free energy barrier of ~ 1.1 kcal/mol. Also, the population of mostly disordered morphologies (<5% β -strand) is larger. In addition, D23N enhances the population of $\text{A}\beta$ morphologies with 25–35% β -strand propensities. On the other hand, the number of hydrophobic contacts per hydrophobic residue is mostly unaffected.

DISCUSSION

Direct experimental atomic-level information on the dimer of the $\text{A}\beta$ protein is not available because trapping a specific transient oligomer is extremely challenging in aqueous solution.^{6,8,18} Although computational studies can fill this gap, very few simulations were done on the aggregation of the full-length $\text{A}\beta$

Table 4. Secondary Structure of $\text{A}\beta_{42}$ Dominant Morphologies (Same as Footnote *a* of Table 3)

cluster no.	clusters in Figure 4		clusters in Figure 5	
	res. no. (chain no.)	motif	res. no. (chain no.)	motif
1	22–27 (#2)	α	2–6 (#1)/12–14 (#1)	a.-p. β
	2–6 (#1)/10–14 (#1)	a.-p. β	2–6 (#2)/10–14 (#2)	a.-p. β
	19–23 (#1)/28–30 (#1)	a.-p. β	17–19 (#2)/30–32 (#2)	a.-p. β
	2–6 (#2)/10–14 (#2)	a.-p. β		
	17–19 (#2)/30–32 (#2)	a.-p. β		
2	2–6 (#1)/10–14 (#1)/25–28 (#2)	a.-p. β	4–6 (#1)/10–12 (#1)	a.-p. β
	23–24 (#1)/2–6 (#2)/10–14 (#2)	a.-p. β	27–33 (#1)/33–39 (#2)	a.-p. β
			36–37 (#1)/29–30 (#2)	a.-p. β
3	22–27 (#2)	α	40–41 (#1)/25–26 (#2)	a.-p. β
	2–6 (#1)/10–14 (#1)	a.-p. β	2–6 (#2)/10–14 (#2)	a.-p. β
	2–6 (#2)/10–15 (#2)	a.-p. β	7–13 (#1)/30–33 (#2)	a.-p. β
			15–19 (#1)/24–28 (#1)	a.-p. β
4	23–27 (#1)	α	30–37 (#1)/3–13 (#2)	a.-p. β
	21–27 (#2)	α	15–18 (#2)/25–28 (#2)	a.-p. β
	2–6 (#1)/10–14 (#1)	a.-p. β	2–6 (#1)/12–14 (#1)	a.-p. β
	2–6 (#2)/10–14 (#2)	a.-p. β	2–6 (#2)/10–14 (#2)	a.-p. β
5	22–26 (#1)	α	32–33 (#2)/37–38 (#2)	a.-p. β
	2–6 (#1)/12–14 (#1)	a.-p. β	2–6 (#1)/10–14 (#1)	a.-p. β
	2–6 (#2)/10–14 (#2)	a.-p. β	27–41 (#1)/25–39 (#2)	a.-p. β
6	4–6 (#1)/10–12 (#1)	a.-p. β	3–6 (#2)/10–13 (#2)	a.-p. β
	27–33 (#1)/33–39 (#2)	a.-p. β	4–7 (#1)/10–12 (#1)	a.-p. β
	36–37 (#1)/29–30 (#2)	a.-p. β	30–32 (#1)/36–38 (#1)	a.-p. β
	40–41 (#1)/25–26 (#2)	a.-p. β	2–6 (#2)/10–14 (#2)	a.-p. β
	2–6 (#2)/10–14 (#2)	a.-p. β	30–32 (#2)/36–38 (#2)	a.-p. β

Table 5. Secondary Structure of $\text{A}\beta_{40}(\text{D23N})$ Dominant Morphologies (Same as Footnote *a* of Table 3)

cluster no.	clusters in Figure 4		clusters in Figure 5	
	res. no. (chain no.)	motif	res. no. (chain no.)	motif
1	2–3 (#1)/2–5 (#2)/10–12 (#2)	a.-p./p. β	25–28 (#2)/34–37 (#2)	a.-p. β
2			4–7 (#1)/2–6 (#2)/12–14 (#2)	a.-p./p. β
3	2–4 (#1)/2–4 (#2)	a.-p. β	33–36 (#1)/34–37 (#2)	a.-p. β
4	4–6 (#1)/2–6 (#2)/12–14 (#2)	a.-p./p. β	4–6 (#1)/2–6 (#2)/12–14 (#2)	a.-p./p. β
	33–36 (#1)/34–37 (#2)	a.-p. β	25–27 (#1)/35–37 (#1)	a.-p. β
5	25–28 (#2)/34–37 (#2)	a.-p. β	25–28 (#2)/34–37 (#2)	a.-p. β
6	2–4 (#1)/4–6 (#2)	p. β	2–6 (#1)/10–13 (#1)/2–4 (#2)	a.-p./p. β
			28–30 (#1)/37–39 (#1)	a.-p. β

dimer^{20,22,32} and, to our knowledge, only one simulation compares the two wild-type sequences, $\text{A}\beta_{1–40}$ and $\text{A}\beta_{1–42}$.²² Moreover, to our knowledge, no simulation has been performed on the $\text{A}\beta_{1–40}(\text{D23N})$ oligomers. Characterizing the $\text{A}\beta$ dimer is important, as it is the smallest oligomer that can serve as a building block for higher order toxic oligomers¹⁵ and it has itself been recognized as neurotoxic.¹³ Here, following our characterization of the three isolated full-length monomers,²⁹ we simulate the physiologically relevant $\text{A}\beta_{1–40}$, $\text{A}\beta_{1–42}$, and $\text{A}\beta_{1–40}(\text{D23N})$ dimers using the OPEP force field³³ coupled to HT-REMD.³⁴ Our results reveal notable differences and similarities between these alloforms, which we relate to previous studies on $\text{A}\beta$, and they can be summarized as follows.

Dimerization. We first look at the structural changes occurring during $\text{A}\beta$ dimerization by comparing with our previous results on the monomer²⁹ at 300 K using the same protocol and force field. We expect more β -strands in the dimer than the

monomer from CD experiments,¹⁸ as well as T-REMD²³ and DMD²² simulations on $\text{A}\beta_{40}$. In agreement with these works, our results for $\text{A}\beta_{40}$ show a slight increase in the averaged total β -strand propensity upon dimerization (Table 1). This increase is particularly localized at the fibril-loop region and C-terminal, while we observe a destabilization at the N-terminal (residues 10–16), as shown in Figure 7. Results are similar but of larger magnitude for the $\text{A}\beta_{40}(\text{D23N})$ dimer: the β -strand propensity is also reduced at the N-terminal and increased at the C-terminal, suggesting a shift of β -strands from the N-terminal to the C-terminal during dimerization for both $\text{A}\beta_{40}$ and $\text{A}\beta_{40}(\text{D23N})$. It is in $\text{A}\beta_{42}$, however, that the difference is the largest, as this alloform exhibits a significant increase of β -strand propensity in all regions, leading to a more significant organization at this level. Overall, we observe an important role for the C-terminal during the dimerization, as it adopts a more extended conformation that favors greatly the formation of β -strands (Figure 7).

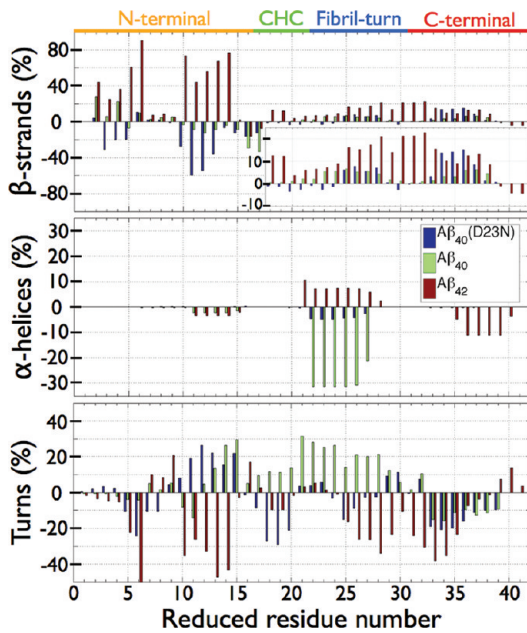


Figure 7. Per residue secondary structure difference between the dimer and the monomer. From top to bottom, β -strands, α -helices, and turn propensities differences for $A\beta_{40}$ (green), $A\beta_{42}$ (red), and $A\beta_{40}(\text{D23N})$ (blue). The percentages shown represent % in the dimer minus % in the monomer.

We also observe that $A\beta$ dimerization for these three alloforms is characterized by a global increase in hydrophobic contacts particularly between the CHC/CHC, CHC/C-terminal, and C-terminal/C-terminal regions (Figure 8). Moreover, the solvent accessible surface area of the CHC and C-terminal residues for these three alloforms is significantly reduced in the dimer (panel B of Figure 9). These observations confirm that the hydrophobic residues of the $A\beta$ monomer are not properly buried, as expected from experiments showing that the $A\beta$ monomer is mostly random coil in solution.^{57–60} The dimer formation is then largely driven by the large energy gain associated with the burial of these hydrophobic residues, as confirmed by the formation of a large number of intermolecular hydrophobic contacts and the appearance of more intramolecular contacts for some residues (Figure 8).

Taken together, these results show that intermolecular contacts due to dimerization lead to a more extended peptide particularly at the C-terminal of $A\beta_{40}$, as has been previously seen in a T-REMD simulation.²³ Moreover, we observe that this is generalizable to other alloforms, at least for $A\beta_{42}$ and $A\beta_{40}(\text{D23N})$, and that it might be a common feature of $A\beta$ dimerization. Interestingly, each of these three alloforms exhibits strong intermolecular contacts at the CHC (Figure 8). This common feature could be targeted by chemical compounds interacting with the CHC region to forbid, already during dimerization, the formation of intermolecular hydrophobic contacts there. It would be interesting to see if other alloforms, especially those having a mutation in this region such as $A\beta_{42}(\text{F19P})$,⁶¹ also share this feature.

Dimer Morphologies. Second, we compare the structural features of the $A\beta_{42}$ and $A\beta_{40}(\text{D23N})$ dimers to the $A\beta_{40}$ dimer. Below, we summarize our findings by focusing on the four regions that play a determinant role in $A\beta$ aggregation:⁵ N-terminal (residues 1–16),^{18,30} CHC (residues 17–21),^{56,61,62} fibril-loop (residues 22–29),⁶³ and C-terminal (residues 30–42).⁵⁶

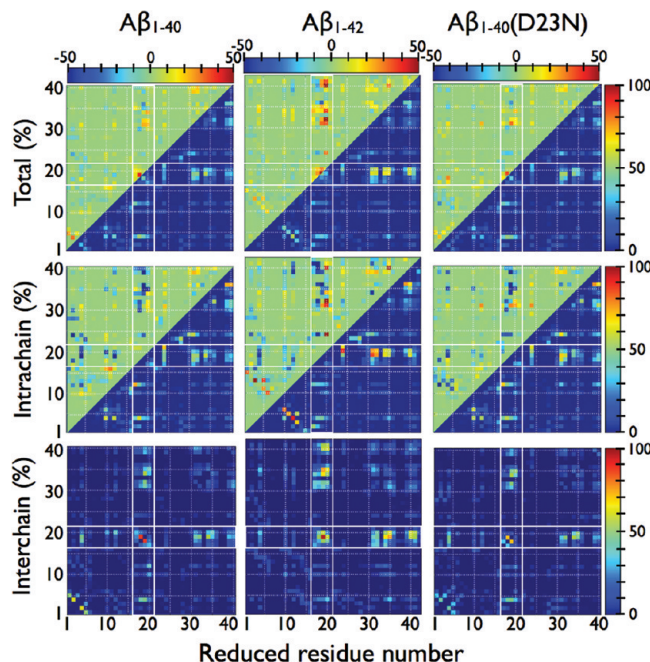


Figure 8. Side chain contact network of the dimer compared to the monomer. The contact maps' lower right corners display the contact propensity of total (first row), intrachain (second row), and interchain (third row) contacts for $A\beta_{40}$ (first column), $A\beta_{42}$ (second column), and $A\beta_{40}(\text{D23N})$ (third column), while the contact maps' upper left corners show the impact of dimerization on the contact propensities from the % in the dimer minus the % in the monomer. The total contact propensity is calculated from % intra plus % inter. The white lines, which are found between residues 16 and 17 and between residues 21 and 22, delimit the CHC region.

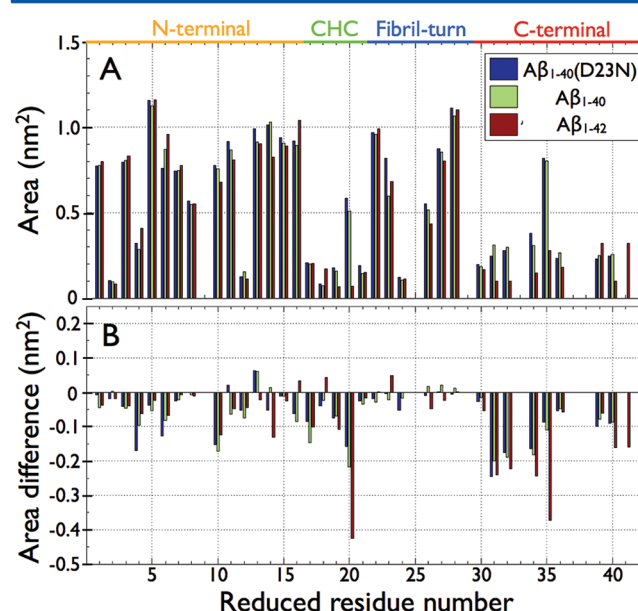


Figure 9. Per residue solvent accessible surface area. (A) In the top panel, the per residue solvent accessible surface area for the $A\beta_{40}$ (green), $A\beta_{42}$ (red), and $A\beta_{40}(\text{D23N})$ (blue) dimers are compared. (B) The surface accessible area differences between the dimer and the monomer are shown in the lower panel. Surface area differences are obtained from the dimer % minus the monomer %.

The N-terminal is unstructured in both $A\beta_{40}$ and $A\beta_{42}$ fibril morphologies,^{9,10} but a recent study combining experiments

and simulations shows otherwise for an annular, transient morphology of $\text{A}\beta_{42}$.³⁰ In this morphology, these authors observed that the N-terminal is found to form intermolecular β -sheets with other N-terminals and it interacts with the fibril-loop region, suggesting an important role for the N-terminal segment of $\text{A}\beta$, which is nonetheless discarded in most simulations. For the monomer, some simulations showed that $\text{A}\beta_{42}$ might form β -hairpin motifs at the N-terminal^{26,29} or form β -sheets with other parts of the peptide.^{22,28}

Our results show a complex role for the N-terminal in the dimer. While the N-terminal of $\text{A}\beta_{42}$ adopts very often a β -hairpin motif, the N-terminal of $\text{A}\beta_{40}$ and $\text{A}\beta_{40}(\text{D}23\text{N})$ populates mostly random coil configurations or small intra- and intermolecular β -sheets, as shown in Figures 2 and 4, in agreement with a previous DMD simulation on the $\text{A}\beta_{40}$ dimer.²² Compared to this same study, it seems that OPEP overestimates the β -sheet propensity at the N-terminal of $\text{A}\beta_{42}$.²² However, a recent MC simulation showed otherwise, as the N-terminal of $\text{A}\beta_{42}$ populates a β -hairpin centered at residues 14–15 with a probability of 74–82%, while we found a hairpin centered at residues 7–9. No experimental results on the structural ensemble of the $\text{A}\beta_{42}$ dimer is available, to our knowledge, that could settle this matter.

The N-terminal is localized at the surface of the protein, and it creates an interface between the solvent and the hydrophobic residues of the CHC and C-terminal (Figures 4 and 5), reducing their solvent accessibility. The solvent accessible surface area (SASA) per residue including the N-terminal is shown in Figure 9. We observe that the hydrophilic N-terminal and fibril-loop region are mainly exposed to the solvent, except for residues Ala2, Val12, and Val24 in all alloforms. While the hydrophobic CHC and C-terminal regions are essentially buried, their SASA is lower in $\text{A}\beta_{42}$ than $\text{A}\beta_{40}$; the variant D23N, on the other hand, is very similar to wild-type $\text{A}\beta_{40}$. To quantify the screening done by the N-terminal on these regions, we recalculated the SASA per residue without considering the N-terminal (residues 1–16). The results clearly show that the N-terminal is responsible in part for shielding the CHC and the C-terminal, as well as the charged residues D23 and K28 in each alloform (Supp. Figure 3, Supporting Information). This shielding is least important for $\text{A}\beta_{42}$, suggesting a greater intrinsic stability for its hydrophobic core. To unveil the origin of the lower SASA of the CHC and C-terminal of the $\text{A}\beta_{42}$ dimer, we recalculated again the SASA without considering Ile41 and Ala42, which are the only difference between $\text{A}\beta_{42}$ and $\text{A}\beta_{40}$. Surprisingly, their direct impact on SASA is not more important than the N-terminal (Supp. Figure 4, Supporting Information); instead, their effect on the tertiary structure is caused indirectly by an overall increase of hydrophobic contact propensities (Figure 3).

Taken together, our results on the N-terminal show that this region is important to shield the CHC and C-terminal hydrophobic residues from the solvent. In the $\text{A}\beta_{42}$ dimer, its role seems secondary compared to the impact of Ile41-Ala42 on the tertiary structure folding in agreement with a previous experiment showing that $\text{A}\beta_{42}$ early oligomerization is weakly impacted by the truncation of the N-terminal residues 1–10, as opposed to $\text{A}\beta_{40}$, and that it is strongly impacted by the truncation of Ile41 and Ala42, $\text{A}\beta_{42}\Delta(41–42)$.⁵

The fibril-loop region has been suggested to be important during nucleation, as a preformed salt-bridge between D23–K28 was shown to greatly enhance the nucleation and fibrillation rates of $\text{A}\beta_{1–40}$.⁶³ Focusing on the $\text{A}\beta_{21–30}$ fragment,

experiments show the presence of a turn between residues 24 and 28 that populates two main conformations with a salt-bridge between K28 and D23 or K28 and E22.⁶⁴ These salt-bridge populations could have been overestimated,⁶⁵ however, and while computational studies on the full-length $\text{A}\beta$ monomer also showed the presence of these two salt-bridges, the 21–30 segment was found to be rather polymorphic, suggesting that further stabilization of this contact is needed during oligomerization.^{28,29}

Here, we observe that the fibril-loop region remains polymorphic in the dimer, visiting α -helix, β -strand, turn, and random coil conformations. The D23–K28 contact is still populated in the WT dimer, but its propensity is reduced compared to the monomer (Table 2). This contact may be easily solvated, like in the monomer, since both D23 and K28 are still highly accessible to the solvent (Figure 9). This observation has to be contrasted against a previous simulation on the $\text{A}\beta_{10–35}$ in which it was observed that dimerization slightly reduces the D23–K28 salt-bridge solvent accessibility.⁶⁶ However, these authors also observed that the salt-bridge can still be easily solvated without a Lactam bridge construct between D23 and K28. Taken together, their results and ours suggest that further stabilization of the D23–K28 salt-bridge and the fibril-loop occur at a later stage of assembly. For $\text{A}\beta_{40}(\text{D}23\text{N})$, as expected, the neutralized side-chain of residue 23 has a significantly smaller contact propensity with K28, which becomes less constrained and does not show a significantly higher contact propensity with the other negatively charged residues in $\text{A}\beta$ (Table 2). Surprisingly, this additional freedom due to a single point mutation is sufficient to stabilize the formation of β -strands at the C-terminal as discussed below.

Both the CHC and the C-terminal are known to play an important role during oligomerization^{5,15,61} and fibrillation^{9,10,17,30} through the formation of extended conformations and β -sheets.⁵⁶ Previous experiments and simulations have shown that the C-terminal of the $\text{A}\beta_{42}$ monomer is more extended than $\text{A}\beta_{40}$.^{22,28,29,57,58} Similar observations were also made for the CHC.^{29,59} These regions were also shown to be important to modulate the tertiary structure of the $\text{A}\beta_{42}$ monomer.^{19,26}

Here, our results suggest that these two regions in the dimer are significantly more extended with higher β -strand and lower turn propensities in $\text{A}\beta_{42}$ than in $\text{A}\beta_{40}$ (Figure 2). (1) The C-terminal of $\text{A}\beta_{42}$ is involved in more diverse β -stranded motifs with higher propensities than in $\text{A}\beta_{40}$ (Figures 2, 4, and 5 and Tables 3 and 4). For example, the second and fifth clusters of Figure 5 exhibit a β -sheet at the C-terminal that is laterally accessible to the solvent on one side. This motif, which is not observed for $\text{A}\beta_{40}$, could promote $\text{A}\beta_{42}$ early oligomerization and be important during nucleation by favoring the recruitment of a third chain at the C-terminal level to elongate the β -sheet in a morphology similar to the fibril morphology: parallel β -sheet made of the C-terminal of each $\text{A}\beta$ peptide.^{9,30} More investigation will be needed to clarify the role of this motif in the assembly of higher order oligomers. (2) The CHC of $\text{A}\beta_{42}$ is involved in β -stranded motifs with the C-terminal (first cluster in Figure 4) as opposed to $\text{A}\beta_{40}$ that is almost unstructured there (Figure 2). This region is also involved in significantly more contacts in $\text{A}\beta_{42}$ (Figure 3). The CHC thus appears more important in $\text{A}\beta_{42}$ than in $\text{A}\beta_{40}$, and we expect that mutations in this region would have a greater impact on $\text{A}\beta_{42}$. Interestingly, Bitan et al. observed experimentally that mutations at the CHC strongly disturb $\text{A}\beta_{42}$ early oligomerization, whereas $\text{A}\beta_{40}$ is only weakly affected.⁵

Moreover, these authors showed that the opposite is observed when the negatively charged Glu22 or Asp23 is mutated. These observations support our results, which show that these two residues are involved in fewer interactions with the positively charged K28 in $\text{A}\beta_{42}$ than in $\text{A}\beta_{40}$ (Table 2). The C-terminal residues Ile41 and Ala42 are thus critical to the $\text{A}\beta_{42}$ dimer morphologies by enhancing the overall β -strand and hydrophobic contact propensities and decreasing the electrostatic contact propensities.

In our simulations, the $\text{A}\beta_{40}(\text{D23N})$ dimer exhibits structural motifs that differ from those observed in both $\text{A}\beta_{40}$ and $\text{A}\beta_{42}$. While its C-terminal has a higher β -strand propensity than in $\text{A}\beta_{40}$, its CHC is almost devoid of any secondary structure as opposed to $\text{A}\beta_{42}$. Its main morphologies are rather unstructured, but some exhibit interesting structural motifs that are weakly populated in the $\text{A}\beta_{40}$ ensemble with, for example, an intermolecular antiparallel β -sheet at the C-terminal (fourth cluster in Figure 4 and other less populated clusters). This motif, which appears already in the dimer, could be important for the nucleation of $\text{A}\beta_{40}(\text{D23N})$, as some of its fibril morphologies are characterized by antiparallel, instead of the common parallel, β -sheets at the C-terminal.¹⁷

Comparison to Previous Studies. Our results on the full-length $\text{A}\beta_{40}$ and $\text{A}\beta_{42}$ dimers can be compared to the other three published folding simulations on these alloforms.^{20,22,32}

Our results on the $\text{A}\beta_{40}$ dimer can be compared to the results of Takeda et al.^{23,32} obtained using the CHARMM19 force field with the SASA implicit solvent model coupled to REMD. In terms of secondary structure, Takeda et al. observed 6% β -strand, 19% α -helix, and 49% turn for their $\text{A}\beta_{10-40}$ structural ensemble²³ and they later observed that the structural ensemble is weakly impacted by the addition of residues 1–9,³² whereas we found higher β -strand (12.6%) and very low α -helix (1.3%) propensities. Turn propensity is however similar (them: 49% vs us: 44.8%). Their contact network is also different with most of the intermolecular contacts being between the N-terminal and the rest of the sequence, whereas we observe high intermolecular contact densities between the CHC and the C-terminal and between the CHC of the two chains (their Figure 5 vs our Figure 2).

Our $\text{A}\beta_{42}$ dimer simulation can be compared to the recent work of Mitternacht et al.²⁰ that used an all-atom force field with implicit solvent representation coupled to Monte Carlo. In terms of secondary structure, these authors observed that the $\text{A}\beta_{42}$ dimer marginally populates α -helices, and mostly adopts antiparallel β -sheet configurations, in agreement with our observations (their text vs our Figure 2 and Tables 1 and 4). Similarly to us, they observed that the turn distribution is localized at residues 7–10 (us: 7–9), 14–15 (us: no), 20–21 and 25–26 (us: 21–24), and 35–38 (us: 36–39), where we consider a turn when its propensity is at least 50%. In terms of intramolecular contacts, their results show that the C-terminal/C-terminal and CHC/C-terminal regions have high contact densities, agreeing with us; however, their region of highest contact density, between CHC and residues 9–12, is absent in our simulation (their Figure 3 vs our Figure 3). Their interchain contacts are also similar to ours with the highest densities being between the C-terminal/C-terminal, the CHC/CHC, and the C-terminal/CHC regions. Their C-terminal/CHC intermolecular contact propensities are, however, less populated than ours. In their simulation, the contact D23–K28 is populated ~30–40% of the time, which is less than in our simulation (53.5%). Finally, their six dominant clusters display similar β -sheet

interactions to our clusters: C-terminal/C-terminal (intra), N-terminal/fibril-loop (intra), CHC/C-terminal (intra), and C-terminal/fibril-loop (intra) (their Figure 6 vs our Figures 4 and 5). We observe more intermolecular β -sheet motifs though, and our β -sheets are shorter in most cases.

The impact of adding two residues to $\text{A}\beta_{40}$ was also studied by Urbanc et al.²² with a four-bead coarse-grained force field with implicit solvent representation coupled to DMD simulations. In terms of secondary structure, their results show higher β -strand propensities at the CHC and at the C-terminal in $\text{A}\beta_{42}$ than in $\text{A}\beta_{40}$ (their Figure 6 vs our Figure 2), in agreement with our results. Their turn distributions for $\text{A}\beta_{40}$ and $\text{A}\beta_{42}$ are similar to ours except at residues 36–39 for which we observe similar turn propensity for these two alloforms (~80%), whereas they observe lower propensity for $\text{A}\beta_{40}$ (~40%) (their Figure 7 vs our Figure 2). They also found a marginal population of α -helices, in agreement with our results. In terms of contact network, our results agree on the following regions of high contact density for both alloforms: CHC/CHC (intermolecular), CHC/C-terminal (inter- and intramolecular), and C-terminal/C-terminal (intramolecular) (their Figures S6 and S7 vs our Figure 3). On the other hand, our results show smaller contact propensity involving the N-terminal (intra- and intermolecularly) and the C-terminal/C-terminal (intermolecularly). Finally, in terms of solvent accessible surface area, they observed that the $\text{A}\beta_{42}$ and $\text{A}\beta_{40}$ dimers have almost the same solvent accessibility per residue as opposed to our results showing that $\text{A}\beta_{42}$ residues at the CHC and at the C-terminal are more buried than in $\text{A}\beta_{40}$ (their Figure S5 vs our Figure 9).

Overall, we see that some of our results on $\text{A}\beta_{40}$ and $\text{A}\beta_{42}$ agree with previous computational studies; however, there are variabilities concerning the net propensities of contacts, secondary structures, and solvent accessible area that are associated with the various force fields and simulation conditions used. Ultimately, new experimental studies will help to validate these simulations.

Role of the Dimer on Oligomerization. In light of our results, we now analyze the role that the $\text{A}\beta$ dimer could have in further oligomerization. Recent experiments showed that the early oligomerization of $\text{A}\beta_{40}$ and $\text{A}\beta_{42}$ differ markedly due to structural differences already present at the dimer and tetramer levels.¹⁵ Our simulations show that the $\text{A}\beta_{42}$ dimer ensemble is energetically more favorable, with more hydrophobic contacts, less solvent accessible surface area for the CHC and C-terminal, and more secondary structure motifs than the $\text{A}\beta_{40}$ dimer ensemble. This suggests that, at later stages of assembly, $\text{A}\beta_{40}$ will need to form more intermolecular hydrophobic contacts to reduce their solvent accessible surface area. We can then expect the $\text{A}\beta_{40}$ tetramer to be dominated by collapsed and rather amorphous conformations. Our results for the $\text{A}\beta_{42}$ dimer show, on the contrary, that it is dominated by configurations with few unfavorable solvent accessible hydrophobic residues, suggesting that the $\text{A}\beta_{42}$ tetramer could easily adopt more open and structured configurations. This agrees with what has been observed and hypothesized in the aforementioned experiment;¹⁵ namely, the $\text{A}\beta_{42}$ tetramer is more open; $\text{A}\beta_{40}$ is more globular. The globular aspect of the $\text{A}\beta_{40}$ tetramer was also observed from recent folding simulations.^{22,67} Fewer numerical results exist for the $\text{A}\beta_{42}$ tetramer, and folding has only been studied using DMD simulation which shows, contrary to the previously mentioned experimental results, that the $\text{A}\beta_{42}$ oligomers populate globular configurations.²² Other molecular dynamic simulations on the folding of $\text{A}\beta_{40}$ and $\text{A}\beta_{42}$ using the same simulation protocol as a benchmark and sampling

enhancing techniques such as HT-REMD will be needed to evaluate more carefully the role of the dimer in the formation of the tetramer morphologies as well as the structural features characterizing them.

Finally, it is known experimentally that both D23N and $A\beta_{42}$ favor the appearance of higher-order oligomers⁵ with an increased fibrillation rate as compared to $A\beta_{40}$.^{9,17} Our results suggest that the origin of this behavior is distinct for $A\beta_{42}$ and $A\beta_{40}$ (D23N), as they exhibit very different structural motifs already at the dimer level, even if we had previously identified similarities between their monomers.²⁹ Formation of β -strands at the CHC is crucial to the oligomerization of $A\beta$, but the D23N alloform, as discussed above, does not have β -strand at the CHC, as opposed to $A\beta_{42}$, hinting that this motif might be important later on during $A\beta_{40}$ (D23N) oligomerization/fibrillation. The fibril-loop region of both alloforms has also different contact and secondary structure propensities (Table 2 and Figure 2, respectively). Moreover, $A\beta_{42}$ displays significantly more hydrophobic interactions than $A\beta_{40}$ (D23N) (Figure 3). These differences lead us to think that diverse and independent structural features may favor the oligomerization and fibrillation of $A\beta$. The different mechanisms of $A\beta$ assembly—formation of extended structures at the CHC and C-terminal through β -sheet,⁵⁶ a salt-bridge between D23 and K28,⁶³ a loop between residues 22–29 and the strand-loop-strand motif^{9,10,17}—would thus happen at different stages of aggregation and have distinct predominance for different alloforms.

CONCLUSION

In this study, we analyzed in detail the impact of dimerization on the secondary and tertiary structures of three physiologically relevant $A\beta$ alloforms: $A\beta_{1-40}$, $A\beta_{1-42}$, and $A\beta_{1-40}$ (D23N). Our study combines secondary structure and contact propensities, free energy landscapes, solvent accessible surface, and clustering. Our simulations clarify the role of Ile41 and Ala42 and D23N on the dimerization of the $A\beta$ peptide.

For $A\beta_{1-42}$, the two additional hydrophobic residues at the C-terminal, Ile41 and Ala42, have a strong impact on folding. They increase the overall hydrophobic contact and β -strand propensities, and reduce the presence of electrostatic contacts as well as the solvent accessibility of the residues at the CHC and C-terminal. The C-terminal of $A\beta_{1-42}$ is also involved in more diverse interactions with the other parts of the peptide. Morphologies with globally higher β -strand and hydrophobic contact propensities are favored, as shown by the free energy analysis.

The mutation D23N enhances the conformational freedom of the positively charged K28, causing, surprisingly, an increase of β -strand propensity at the C-terminal relative to the wild-type $A\beta_{1-40}$. While its predominant morphologies are rather unstructured with no secondary structure at the CHC, the presence of β -stranded motifs at the C-terminal such as an intermolecular antiparallel β -sheet, whose population is marginal in the $A\beta_{1-40}$ morphological ensemble, could be important to facilitate nucleation. In addition, the free energy landscape of the D23N variant shows that this alloform increases the population of configurations with larger β -strand propensities relative to the wild-type $A\beta_{1-40}$.

Overall, our results reveal that oligomers as small as the dimer of these three alloforms already have very different structural motifs, suggesting different oligomerization pathways in agreement with previous experiments on $A\beta$. They also emphasize that more simulations on higher order oligomers, using enhancing

sampling algorithms such as HT-REMD, will be needed to further understand the role of the dimer in later stages of assemblies and how the oligomerization is impacted by the distinct structural features of different $A\beta$ alloforms.

ASSOCIATED CONTENT

S Supporting Information

Table showing the Pearson correlation coefficients comparing the monomers chemical shifts to experiment and figures showing monomers chemical shifts per residue, time evolution of the secondary structure of $A\beta_{1-42}\Delta(41-42)$, and SASA without N-terminal or Ile41–Ala42. This material is available free of charge via the Internet at <http://pubs.acs.org>.

AUTHOR INFORMATION

Corresponding Author

*E-mail: normand.mousseau@umontreal.ca.

Notes

The authors declare no competing financial interest.

ACKNOWLEDGMENTS

This work was funded in part by the Canada Research Chairs program, the Fonds québécois de recherche sur la nature et les technologies (FQRNT), the Natural Sciences and Engineering Research Council of Canada (NSERC), and the Fonds de recherche en santé du Québec (FRSQ). Calculations were done on the computers of Calcul Québec. Financial support of CNRS and the Institut Universitaire de France is also acknowledged.

REFERENCES

- (1) Selkoe, J. D. *Nature* **2003**, *426*, 900–904.
- (2) Morgan, C.; Colombres, M.; Nunez, M. T.; Inestrosa, N. C. *Prog. Neurobiol.* **2004**, *74*, 323–349.
- (3) Walsh, D.; Selkoe, D. J. *J. Neurochem.* **2007**, *101*, 1172–1184.
- (4) Irvine, G. B.; El-Agnaf, O. M.; Shankar, G. M.; Walsh, D. M. *Mol. Med.* **2008**, *14*, 451–464.
- (5) Bitan, G.; Vollers, S. S.; Teplow, D. B. *J. Biol. Chem.* **2003**, *278*, 34882–34889.
- (6) Bitan, G.; Kirkkitadze, M. D.; Lomakin, A.; Vollers, S. S.; Benedek, G. B.; Teplow, D. B. *Proc. Natl. Acad. Sci. U.S.A.* **2003**, *100*, 330–335.
- (7) Chen, Y.-R.; Glabe, C. G. *J. Biol. Chem.* **2006**, *281*, 24414–24422.
- (8) Kirkkitadze, M. D.; Condron, M. M.; Teplow, D. B. *J. Mol. Biol.* **2001**, *312*, 1103–1119.
- (9) Luhrs, T.; Ritter, C.; Adrian, M.; Riek-Lohr, D.; Bohrmann, B.; Dobeli, H.; Schubert, D.; Riek, R. *Proc. Natl. Acad. Sci. U.S.A.* **2005**, *102*, 17342–17347.
- (10) Tycko, R. *Q. R. Biophys.* **2006**, *39*, 1–55.
- (11) Sakono, M.; Zako, T. *FEBS J.* **2010**, *277*, 1348–1358.
- (12) Haass, C.; Selkoe, D. J. *Nat. Rev. Mol. Cell Biol.* **2007**, *8*, 101–112.
- (13) Shankar, G. M.; Li, S.; Mehta, T. H.; Garcia-Munoz, A.; Shepardson, N. E.; Smith, I.; Brett, F. M.; Farrell, M. A.; Rowan, M. J.; Lemere, C. A.; Regan, C. M.; Walsh, D. M.; Sabatini, B. L.; Selkoe, D. J. *Nat. Med.* **2008**, *14*, 837–842.
- (14) Kumar-Singh, S.; Theuns, J.; Van Broeck, B.; Pirici, D.; Vennekens, K.; Corsmit, E.; Cruts, M.; Dermaut, B.; Wang, R.; Van Broeckhoven, C. *Hum. Mutat.* **2006**, *27*, 686–695.
- (15) Bernstein, S.; Dupuis, N. F.; Lazo, N. D.; Wyttenbach, T.; Condron, M. M.; Bitan, G.; Teplow, D. B.; Shea, J.-E.; Ruotolo, B. T.; Robinson, C. V.; Bowers, M. T. *Nat. Chem.* **2009**, *1*, 326–331.
- (16) Grabowski, T. J.; Cho, H. S.; Vonsattel, J. P. G.; Rebeck, G. W.; Greenberg, S. M. *Ann. Neurol.* **2001**, *49*, 697–705.
- (17) Tycko, R.; Sciarretta, K. L.; Orgel, J. P. R. O.; Meredith, S. C. *Biochemistry* **2009**, *48*, 6072–6084.

- (18) Ono, K.; Condron, M. M.; Teplow, D. B. *J. Biol. Chem.* **2010**, *285*, 23186–23197.
- (19) Mitternacht, S.; Staneva, I.; Hard, T.; Irback, A. *Proteins* **2010**, *78*, 2600–2608.
- (20) Mitternacht, S.; Staneva, I.; Hard, T.; Irback, A. *J. Mol. Biol.* **2011**, *410*, 357–367.
- (21) Urbanc, B.; Cruz, L.; Yun, S.; Buldyrev, S. V.; Bitan, G.; Teplow, D. B.; Stanley, H. E. *Proc. Natl. Acad. Sci. U.S.A.* **2004**, *101*, 17345–17350.
- (22) Urbanc, B.; Betnel, M.; Cruz, L.; Bitan, G.; Teplow, D. *J. Am. Chem. Soc.* **2010**, *132*, 4266–4280.
- (23) Takeda, T.; Klimov, D. K. *Proteins* **2009**, *77*, 1–13.
- (24) Chebaro, Y.; Mousseau, N.; Derreumaux, P. *J. Phys. Chem. B* **2009**, *113*, 7668–7675.
- (25) Lu, Y.; Wei, G.; Derreumaux, P. *J. Phys. Chem. B* **2011**, *115*, 1282–1288.
- (26) Mitternacht, S.; Staneva, I.; Irback, A. *J. Mol. Biol.* **2011**, *410*, 357–367.
- (27) Sgourakis, N. G.; Yan, Y.; McCallum, S.; Wang, C.; Garcia, A. E. *J. Mol. Biol.* **2007**, *368*, 1448–1457.
- (28) Yang, M.; Teplow, D. B. *J. Mol. Biol.* **2008**, *384*, 450–464.
- (29) Cote, S.; Derreumaux, P.; Mousseau, N. *J. Chem. Theory Comput.* **2011**, *7*, 2584–2592.
- (30) Miller, Y.; Ma, B.; Tsai, C.-J.; Nussinov, R. *Proc. Natl. Acad. Sci. U.S.A.* **2010**, *107*, 14128–14133.
- (31) Fradinger, E.; Monien, B.; Urbanc, B.; Lomakin, A.; Tan, M.; Li, H.; Spring, S.; Condron, M.; Cruz, L.; Xie, C.-W.; Benedek, G.; Bitan, G. *Proc. Natl. Acad. Sci. U.S.A.* **2008**, *105*, 14175–14180.
- (32) Takeda, T.; Klimov, D. K. *J. Phys. Chem. B* **2009**, *113*, 6692–6702.
- (33) Maupetit, J.; Tuffery, P.; Derreumaux, P. *Proteins* **2007**, *69*, 394–408.
- (34) Laghaei, R.; Mousseau, N.; Wei, G. *J. Phys. Chem. B* **2010**, *114*, 7071–7077.
- (35) Sugita, Y.; Okamoto, Y. *Chem. Phys. Lett.* **1999**, *314*, 141–151.
- (36) Fukunishi, H.; Watanabe, O.; Takada, S. *J. Chem. Phys.* **2002**, *116*, 9058–9067.
- (37) Berendsen, H. J. C.; Postma, J. P. M.; van Gunsteren, W. F.; DiNola, A.; Haak, J. R. *J. Chem. Phys.* **1984**, *81*, 3684–3690.
- (38) Andersen, H. C. *J. Comput. Phys.* **1983**, *52*, 24–34.
- (39) Maupetit, J.; Derreumaux, P.; Tuffery, P. *J. Comput. Chem.* **2010**, *31*, 726–738.
- (40) Maupetit, J.; Derreumaux, P.; Tuffery, P. *Nucleic Acids Res.* **2009**, *37* (web server issue), W498–503.
- (41) Derreumaux, P.; Mousseau, N. *J. Chem. Phys.* **2007**, *126*, 025101.
- (42) Chebaro, Y.; Dong, X.; Laghaei, R.; Derreumaux, P.; Mousseau, N. *J. Phys. Chem. B* **2009**, *113*, 267–274.
- (43) Laghaei, R.; Mousseau, N.; Wei, G. *J. Phys. Chem. B* **2011**, *115*, 3146–3154.
- (44) Laghaei, R.; Mousseau, N. *J. Chem. Phys.* **2010**, *132*, 165102.
- (45) Nasica-Labouze, J.; Meli, M.; Derreumaux, P.; Colombo, G.; Mousseau, N. *PLoS Comput. Biol.* **2011**, *7*, e1002051.
- (46) Melquiond, A.; Mousseau, N.; Derreumaux, P. *Proteins* **2006**, *65*, 180–191.
- (47) Chen, W.; Mousseau, N.; Derreumaux, P. *J. Chem. Phys.* **2006**, *125*, 084911.
- (48) Dong, X.; Chen, W.; Mousseau, N.; Derreumaux, P. *J. Chem. Phys.* **2008**, *128*, 125108.
- (49) Melquiond, A.; Dong, X.; Mousseau, N.; Derreumaux, P. *Curr. Alzheimer Res.* **2008**, *5*, 244–250.
- (50) Wei, G.; Mousseau, N.; Derreumaux, P. *Prion* **2007**, *1*, 3–8.
- (51) Frishman, D.; Argos, P. *Proteins: Struct., Funct., Genet.* **1995**, *23*, S66–S79.
- (52) Daura, X.; Suter, R.; van Gunsteren, W. F. *J. Chem. Phys.* **1999**, *110*, 3049–3055.
- (53) Eisenhaber, F.; Lijnzaad, P.; Argos, P.; Sander, C.; Scharf, M. *J. Comput. Chem.* **1995**, *16*, 273–284.
- (54) Krivov, G. G.; Shapovalov, M. V.; Dunbrack, R. L. Jr. *Proteins* **2009**, *77*, 778–795.
- (55) Chodera, J. D.; Swope, W. C.; Pitera, J. W.; Seok, C.; Dill, K. A. *J. Chem. Theory Comput.* **2007**, *3*, 26–41.
- (56) Liu, R.; McAllister, C.; Lyubchenko, Y.; Sierks, M. *J. Neurosci. Res.* **2004**, *75*, 162–171.
- (57) Lim, K. H.; Collver, H. H.; Le, Y. T. H.; Nagchowdhuri, P.; Kenney, J. M. *Biochem. Biophys. Res. Commun.* **2007**, *353*, 443–449.
- (58) Yan, Y.; Wang, C. *J. Mol. Biol.* **2006**, *364*, 853–862.
- (59) Hou, L.; Shao, H.; Zhang, Y.; Li, H.; Menon, N. K.; Neuhaus, E. B.; Brewer, J. M.; Byeon, I.-J. L.; Ray, D.; Vitek, M. P.; Iwashita, T.; Makula, R. A.; Przybyla, A. B.; Zagorski, M. G. *J. Am. Chem. Soc.* **2004**, *126*, 1992–2005.
- (60) Zhang, S.; Iwata, K.; Lachenmann, M. J.; Peng, J. W.; Li, S.; Stimson, E. R.; Lu, Y.-a.; Felix, A. M.; Maggio, J. E.; Lee, J. P. *J. Struct. Biol.* **2000**, *130*, 130–141.
- (61) Bernstein, S. L.; Wyttenbach, T.; Baumketner, A.; Shea, J.-E.; Bitan, G.; Teplow, D. B.; Bowers, M. T. *J. Am. Chem. Soc.* **2005**, *127*, 2075–2084.
- (62) Chen, Y.-R.; Huang, H.-B.; Lo, C.-J.; Wang, C.-C.; Su, C.-L.; Liu, H.-T.; Shiao, M.-S.; Lin, T.-H.; Chen, Y.-C. *Biochem. Biophys. Res. Commun.* **2011**, *405*, 91–95.
- (63) Sciarretta, K. L.; Gordon, D. J.; Petkova, A. T.; Tycko, R.; Meredith, S. C. *Biochemistry* **2005**, *44*, 6003–6014.
- (64) Lazo, N. D.; Grant, M. A.; Condron, M. C.; Rigby, A. C.; Teplow, D. B. *Protein Sci.* **2005**, *14*, 1581–1596.
- (65) Baumketner, A.; Bernstein, S. L.; Wyttenbach, T.; Lazo, N. D.; Teplow, D. B.; Bowers, M. T.; Shea, J.-E. *Protein Sci.* **2006**, *15*, 1239–1247.
- (66) Reddy, G.; Straub, J. E.; Thirumalai, D. *J. Phys. Chem. B* **2009**, *113*, 1162–1172.
- (67) Kim, S.; Takeda, T.; Klimov, D. *J. Chem. Phys.* **2010**, *132*, 225101.